

Mechanics of three-dimensional, nonbonded random fiber networksGopinath Subramanian¹ and Catalin R. Picu^{1,2}¹*Scientific Computation Research Center, Rensselaer Polytechnic Institute, Troy, New York 12180-3590, USA*²*Department of Mechanical, Aerospace and Nuclear Engineering, Rensselaer Polytechnic Institute, Troy, New York 12180-3590, USA*

(Received 24 February 2011; published 25 May 2011)

The mechanical behavior of an ensemble of athermal fibers forming a nonbonded network subjected to triaxial compression is studied using a numerical model. The response exhibits a power law dependence of stress on the dilatation strain and hysteresis upon loading and unloading. A stable hysteresis loop results after the first loading and unloading cycle. In the early stages of compaction, strain energy is associated primarily with the bending of fibers, while at higher densities, it is stored primarily in the axial deformation mode. It is shown that the exponent of the power law, and the partition of energy in the axial and bending modes depends on the ratio of the bending to axial stiffness of the fibers. Accounting for interfiber friction does not change the functional form of the stress-strain relationship or the exponent. The central feature that distinguishes the mechanics of this system from that of bonded random networks is the relative sliding at contacts and the ensuing fiber rearrangements. We show that suppressing sliding leads to a much stiffer response. The results indicate that the value of the exponent of the stress-strain power law is determined not only by fiber bending and the formation of new contacts, but also by the relative sliding and axial deformation of fibers.

DOI: 10.1103/PhysRevE.83.056120

PACS number(s): 62.20.F–, 45.70.Cc, 45.70.Vn

I. INTRODUCTION

Structures made from fibers are a common occurrence in both the synthetic and biological worlds. A common example is rubber, which is a cross-linked molecular network [1,2]. Gels are also molecular networks that are swollen by the absorption of water [3]. Polymeric fibers of diameter on the order of several micrometers are used in a variety of consumer products. Nonwovens are made from fibers of high aspect ratio that are not bonded to each other, but entangle and interact frictionally. Nonwovens are used for thermal insulation (e.g., fiberglass and felt), filtration, and sound insulation [4–6]. They are also used for liquid absorption in hygiene products. Paper is one of the oldest manmade materials based on random fiber networks and is made from cellulose fibers obtained from pulp through a wet process.

Many naturally occurring materials, including arterial walls [7], intervertebral discs [8,9], and cellular cytoskeleton [10], are being increasingly understood as complex dynamic structures. In particular, the cytoskeleton, which is responsible for cell locomotion [11], cell division [12], and integrity and viscoelasticity of the cytoplasm [13], has been shown to be a highly dynamic structure that undergoes continual rearrangement [14].

When individual fibers of a network have nanoscale dimensions, such as in molecular networks, thermal fluctuations play an important role in their mechanics, and their mechanical behavior is entropic. Larger fibers are less affected by thermal fluctuations, and their response is enthalpic. These latter networks are referred to as *athermal*. Further classification can be made based on the relative axial and bending stiffness of individual fibers: The high aspect ratio of individual fibers leads to a higher axial stiffness than bending stiffness. If the bending stiffness can be neglected relative to the axial stiffness, fibers are considered *flexible*. In such networks subjected to thermal fluctuations, axial deformation (stretching) entails a reduction of filament entropy before a significant enthalpic contribution is observed. The degree of tortuosity

of the filament is characterized by the persistence length, which indicates the length along the filament beyond which orientation memory is lost. When the persistence length is comparable to the filament length (or the mean segment length in bonded networks), the fiber is considered *semiflexible*.

The mechanics of bonded networks has been studied extensively by both the engineering, and physics communities, and extensive references can be found in reviews [15–17]. In these systems, the bonds, or cross links, are permanent, and the formation of new contacts (i.e., the effect of excluded volume) is usually neglected.

On the other hand, the mechanics of nonbonded, athermal, random networks has received less attention. Some experimental [18–22], and modeling/simulation studies [23–29] are present in the literature. The focus in most cases has been on the response of fiber mats/wads to uniaxial or triaxial compression, motivated by industrial compaction processes. The central feature that governs the mechanical behavior of these entangled (as opposed to cross-linked) systems is the formation of *temporary* contacts between fibers. One theoretical treatment by van Wyk [23] leads to a constitutive model for fiber wads predicting a scaling of stress with density of the form,

$$\sigma = \psi (\rho^n - \rho_{th}^n), \quad (1)$$

where ρ and ρ_{th} are the current and stiffness percolation densities, respectively. The coefficient ψ is proportional to the elastic modulus of the fibers, and the exponent $n = 3$. Toll [26] confirmed this value of n and predicted that for systems in which fibers are preferentially oriented in the plane perpendicular to the direction of compression at the beginning of the deformation, n increases to 5.

In experiments it was observed that the exponent increases with sample mass and takes on values between 2 and 6 [21]. In experiments performed with various types of fibers, significant hysteresis was observed during the loading-unloading cycling. The stress-strain curves eventually overlap on a stable

hysteresis loop after a small number of cycles. Rate sensitivity was also observed and appears to be related to the size of the hysteresis loop [19]. In experiments, as interfiber friction cannot be eliminated, both hysteresis and rate effects have been attributed to fiber rearrangements and to viscous effects at fiber-fiber contacts. In particular, the presence of water is known to significantly influence the mechanics of nonbonded fiber networks. This effect is well-known in granular media, where the constitutive behavior of contacts is likely more important than in fiber networks.

A relatively small number of numerical studies addressing the mechanical behavior of nonbonded networks has been published [19,28–30]. These models are limited in the number and size of fibers considered. Using fibers of aspect ratio 38, Durville [29] obtained results which generally agree with van Wyk’s theory and observed that the number of contacts increased as $\rho^{2/3}$. He also studied the effect of fiber waviness, but for the range of parameters considered in his study, no definite conclusion can be drawn regarding the effect of this parameter. The results by Rodney *et al.* [28] confirm these observations. They used fibers of aspect ratio as high as 100 and concluded that stress follows van Wyk’s prediction of $n = 3$, and that the number of contacts increases linearly with density.

In this study, we examine the mechanical behavior of athermal, nonbonded fiber networks subjected to triaxial compression, focusing on the overall response of the system [functional form, and exponent in Eq. (1)]. In particular, we look at the effect of friction and sliding at fiber contacts. Both these aspects have not been examined in previous numerical studies and are difficult to control/observe in experiments. We show that sliding is an important component of the physics of this system. We also study the effect of the ratio between the fiber bending and axial stiffness on the network behavior and conclude that while the power function form remains valid, the value of the exponent depends on this ratio. The model reproduces the hysteretic behavior and the stabilization after initial cycling observed in experiments.

II. SIMULATION METHOD

Semiflexible fibers are modeled using a modified bead-spring model. As in the classical bead-spring model, contact energy between nonbonded beads is modeled using a shifted and truncated Lennard-Jones potential, given by

$$U_{\text{contact}}(r) = \begin{cases} 4\hat{\epsilon}[(\hat{\delta}/r)^{12} - (\hat{\delta}/r)^6] + \hat{\epsilon}, & r \leq r_c, \\ 0, & r > r_c. \end{cases} \quad (2)$$

We use the symbols $\hat{\delta}$ and $\hat{\epsilon}$ in lieu of the traditional σ and ϵ , as σ is reserved to mean stress and ϵ could potentially mean strain. The fundamental units in this study are m , $\hat{\delta}$, and $\hat{\epsilon}$, where m is the mass of a single bead, and $\hat{\delta}$ and $\hat{\epsilon}$ set the length and energy scales of the simulations. The cutoff distance of the Lennard-Jones potential is chosen as $r_c = 2^{1/6}\hat{\delta}$, making the pairwise interaction potential purely repulsive. This choice of cutoff distance sets the bead diameter and thereby fiber diameter $d = r_c$.

Axial energy is modeled using a harmonic bond potential between consecutive beads, and bending energy of the fiber is

modeled using a harmonic angle potential between triplets of consecutive beads. These energies are given by

$$U_{\text{axial}}(r) = \frac{k_a}{2} (r - d)^2, \quad (3)$$

$$U_{\text{bending}}(r) = \frac{k_b}{2} (\theta - \theta_0)^2. \quad (4)$$

The equilibrium bond length is chosen to be the fiber diameter d , and the equilibrium angle between three consecutive beads is chosen as $\theta_0 = \pi$. (Choosing θ_0 different from π can be used to model crimped fibers.) The coefficients of the interaction potentials in Eqs. (3) and (4) are taken as $k_a = 372.2\hat{\epsilon}/\hat{\delta}^2$, and $k_b = 29.31\hat{\epsilon}$. This choice ensures that for a given fiber with Young’s modulus E , and diameter $d = r_c$, the energy of deformation in Hertzian contact, axial, and bending modes is given by the classical expressions from continuum mechanics (see the Appendix). This relatively large value of k_a minimizes effects of fiber surface roughness. Using a harmonic bond for the axial stiffness has been shown to minimize the possibility of fiber crossing [31–33] and is further reduced by the high value of k_a . The volume of a fiber is taken to be the volume of an equivalent cylinder, with two hemispherical caps. At any given point of time, the volumetric density ρ is the ratio of the volume of all fibers to the volume of the simulation box.

Coulomb friction is introduced between contacting, nonbonded beads that move relative to each other. The coefficient of dynamic friction, that is, the ratio between the friction force and the normal force, is denoted by μ . Dynamic friction is applied in the direction opposite to the relative tangential velocity between beads. Static friction is applied between pairs of beads whose relative velocity is less than $10^{-10}\hat{\delta}^2m^{-0.5}\hat{\epsilon}^{-0.5}$. A small dissipative viscous damping factor $\eta = 0.1$ was introduced for numerical stability. This damping factor, along with the friction serves to cool down the system, and hence, the results discussed are relevant for the athermal limit of the system.

All simulations were run using a modified version of LAMMPS [34], with fibers of aspect ratio 50; the parameters used in these simulations are summarized in Table I. Initial configurations of fibers were obtained by growing straight fibers with random orientations in a cubic simulation box with periodic boundary conditions. In this initial configuration, the volumetric density ρ is low enough to ensure that there are no interactions between fibers. Since fibers are grown at random, there is inevitably some degree of overlap between a small number of fibers, which is removed by an energy minimization. The resulting configuration is then subjected to stepwise triaxial compaction using displacement-imposed boundary conditions. At each step, the simulation box is deformed by a small amount, and the equations of motion are integrated. As a result of the deformation, the fibers gain some energy, and start to move. The size of the simulation box is then held fixed, until the average velocity of the beads drops

TABLE I. Summary of system parameters used.

No. of fibers	Beads/fiber	Fiber length	Sparse box side	Compact box side
1200	50	56.13	509.7	57.0

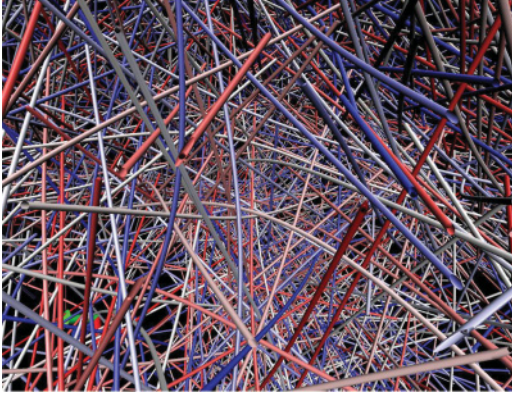


FIG. 1. (Color online) Snapshot of a simulation cell, with fibers depicted as continuous filaments.

below a cutoff value of $1 \times 10^{-5} \hat{\gamma}^2 m^{-0.5} \hat{\rho}^{-0.5}$. The system is then allowed to proceed to the next step of deformation. A snapshot of the fiber network during the compaction process is shown in Fig. 1.

The triaxial compaction is continued until the preset maximum density is reached. The number of fibers in the system is chosen such that at this maximum density, the side of the simulation box is larger than the equilibrium length of a fiber. This is done to ensure that artifacts arising from fibers interacting with themselves across the periodic boundaries are eliminated. Once this maximum density has been attained, the simulation box is subjected to stepwise triaxial expansion, ensuring that the average bead velocity drops below the cutoff at each step. At the end of each step during both compaction and expansion, the configuration of the simulation box is recorded, and the energies of each mode (contact, axial, and bending) are computed.

Stress and dilatation strain for each configuration are computed using the following procedure. The deformation is described by a spherical deformation gradient tensor $\mathbf{F} = q\mathbf{I}$, where \mathbf{I} is the identity matrix, and q is a parameter related to the current density ρ as

$$q = \left(\frac{\rho_0}{\rho} \right)^{1/3}, \quad (5)$$

where ρ_0 is a reference density and is arbitrarily assigned a value of unity. Dilatation is then computed as the trace of the Green strain \mathbf{E} , and is given by

$$\Delta = \mathbf{E}_{ii} = \frac{3}{2}(q^2 - 1). \quad (6)$$

Note that the inverse relationship between ρ and Δ implies that a decreasing value of Δ corresponds to compaction.

The Cauchy stress is evaluated as

$$\mathbf{T} = \frac{1}{\det \mathbf{F}} \mathbf{F} \frac{\partial \hat{U}}{\partial \mathbf{E}} \mathbf{F}^T, \quad (7)$$

where \hat{U} is the total strain energy density. Since the contributions to the total strain energy density is the sum of the individual components ($\hat{U} = \hat{U}_{axial} + \hat{U}_{bending} + \hat{U}_{contact}$), the stresses due to each interaction can be similarly decomposed

as $\mathbf{T} = \mathbf{T}_{axial} + \mathbf{T}_{bending} + \mathbf{T}_{contact}$. The components \mathbf{T}_j are spherical tensors with diagonal elements given by

$$\sigma_j = [T_{ii}]_j = -3 \frac{\rho^2}{\rho_0} \frac{\partial \hat{U}_j}{\partial \rho};$$

$$j \in [axial, bending, contact]. \quad (8)$$

The pressure associated with the Cauchy stress is given by $\sigma = \sigma_{axial} + \sigma_{bending} + \sigma_{contact}$ and is referred to as the total stress.

The average fiber orientation was seen to remain random at all levels of compaction in this study, as evidenced by computing the orientational order parameter,

$$\langle P_2(\cos \beta) \rangle = \left\langle \frac{3 \cos^2 \beta - 1}{2} \right\rangle, \quad (9)$$

where β is the angle made by the end-to-end vector of a fiber and one of the coordinate axes, and the average is taken over all fibers in the system.

III. RESULTS AND DISCUSSION

A. Structural regimes and evolution of stress

As an assembly of fibers is compacted from low-density to high-density, the system progresses through three identifiable regimes. We refer to these regimes as sparse, network, and compacted. The characteristics associated with the transition between regimes are described in this section.

In order to differentiate between the sparse and network regimes, we use the concept of percolation. Geometric percolation is defined as the formation of a continuous path/cluster spanning the entire problem domain. This structure may or may not be sufficiently rigid to provide nonzero elastic moduli on the global scale. Rigidity percolation refers to the critical density at which the structure acquires stiffness. Geometric and rigidity percolation are, in general, distinct events [35]. For a system of initially straight fibers, geometric percolation can be estimated using the results in Bug *et al.* [36] and Balberg *et al.* [37], where it was shown theoretically and numerically that the percolation number density of rods scales as $\phi_{th} \sim R^{-1} L_0^{-2}$, where R is the fiber radius, and L_0 is the fiber length. This relationship is approximate; the approximation becomes better for high aspect ratio fibers. The proportionality constant resulting from the numerical study in Balberg *et al.* [37] is approximately 0.44. Interestingly, the maximum packing number density of spherocylinders is related to the fiber radius and length through an identical relationship with a scaling constant 3.24 [38].

To our knowledge, the stiffness percolation threshold for this system has not been studied systematically. Also, it is not clear that the stiffness percolation threshold for the bulk modulus is identical to that for the shear modulus. In fact, the fragility observed in networks close to percolation indicates that these thresholds may be different. Numerical data for stiffness percolation in triaxial compression (bulk modulus) were reported by Rodney *et al.* [28]. The number density at stiffness percolation was observed to scale as $\phi_{th} \sim R^{-1} L_0^{-2}$, with a proportionality constant of 2.93. Although we did not study the stiffness percolation threshold in detail, our numerical estimates follow these trends.

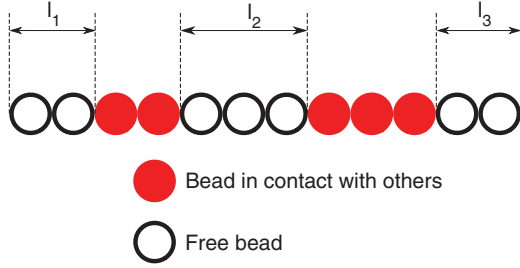
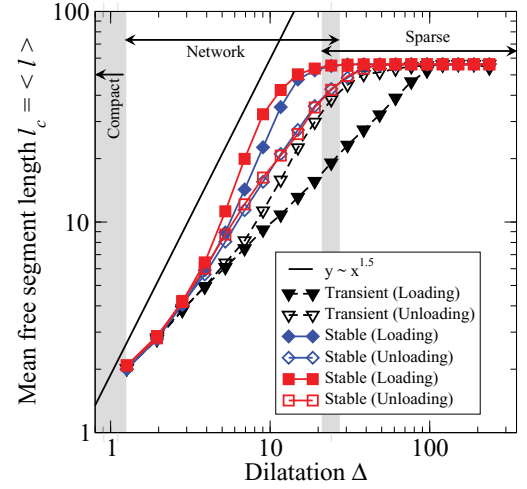


FIG. 2. (Color online) Schematic illustrating the definition of free segment length used in the study. The fiber shown has three free segments of lengths l_1, l_2, l_3 .

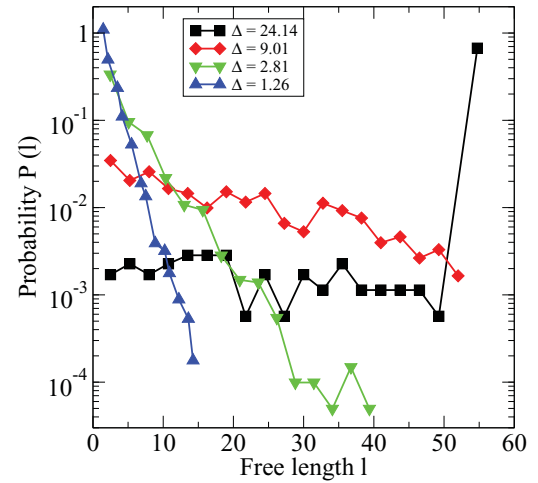
The transition from network to compacted regimes is identified by monitoring the free segment length l . This quantity is the length of segments between two contacts on a fiber and is computed directly from the simulation snapshots, as depicted schematically in Fig. 2. A single fiber can have multiple free segments. The mean free segment length $l_c = \langle l \rangle$ is computed over all free segments l_i . Figure 3(a) shows a plot of l_c as a function of the dilatation strain Δ during compaction. The system evolves during cycling, with parameters being substantially different for the first cycle, and reaching steady state at later stages. The figure shows the evolution of l_c during the first cycle (labeled “Transient”) and two of the stable cycles. We observe that the curve shows pronounced hysteresis, with the network range extending to larger dilatation strains during unloading. Also shown as a straight solid line is $l_c \sim \Delta^{1.5}$, which, for this range of densities, corresponds to $l_c \sim \rho^{-1}$. This line shows the scaling predicted by the Corte-Kallmes theory [24] and is seen to provide a reasonable approximation for the loading branch of the stable cycle in the network regime. As compaction proceeds, as seen in Fig. 3(a), the slope of the l_c vs Δ curve seems to change in the vicinity of $\Delta \approx 2$ ($\rho \approx 0.28$), and $l_c \rightarrow 0$. This change of slope can be associated with a transition that is an indicator of approaching the compacted regime.

The probability density function (PDF) of the free segment length, $P(l)$, for the loading branch of a single stable cycle is shown in Fig. 3(b) at various levels of compaction. Close to the percolation threshold, the PDF is nearly a δ function, centered at $l = L_0$. The probability of finding segments of various lengths is nevertheless nonzero, as a small number of fibers make contact. At higher densities, the distribution is exponential ($P(l) = l_c^{-1} \exp[-l/l_c]$), consistent with a Poisson process where contacts on a fiber are formed at random locations, also discussed in the Corte-Kallmes theory [24]. In the high-compaction limit, $P(l)$ approaches a δ function, centered at zero.

The stress produced in the system was also examined. After the transient loading-unloading cycle, the system evolves to a stable hysteresis loop. The total stress σ , obtained for the first and stable cycles is shown in Fig. 4 for systems with no friction, that is, $\mu = 0$. This hysteretic behavior, also seen in Fig. 3(a), has been observed experimentally [19]. During the transient cycle, the system softens; this phenomenon is commonly observed in fatigue testing of metals that have been hardened (by either prestraining or heat treatment) before



(a)



(b)

FIG. 3. (Color online) (a) Evolution of mean free segment length, l_c , during cycling, shown for the transient cycle, and two stable cycles. Also shown are the approximate boundaries of the three different regimes. (b) Probability density function (PDF) of segment lengths, $P(l)$, at four stages of a stable compaction cycle. The PDF evolves from nearly a δ function at low compactions to exponential, with progressively lower mean.

cycling. For our system, which is frictionless, softening is associated with fiber rearrangements.

The stress-strain curves are power laws for almost two decades of dilatation strain. The loading branch of the transient stress-dilatation curve is fitted to $\sigma \sim \Delta^{-5.03}$, while the corresponding branch of the stable cycle is fitted to $\sigma \sim \Delta^{-5.46}$. These scalings correspond to fits of $\sigma \sim \rho^{3.79}$ and $\sigma \sim \rho^{4.11}$, respectively. Our exponents are larger than van Wyk’s model [23], which, as stated in the Introduction, predicts $\sigma \sim \rho^3$. The larger exponent values are consistent with the departure from theory that is observed in experiments. Exponents ranging from 2 to 6, with the higher values corresponding to samples of larger initial mass are reported [19,21,22]. The values reported here are in agreement with these experimental findings.

The loading branch of the stable stress-dilatation curve was decomposed into its constituents, as in Eq. (8), and the three components are shown in Fig. 5. The total stress is dominated

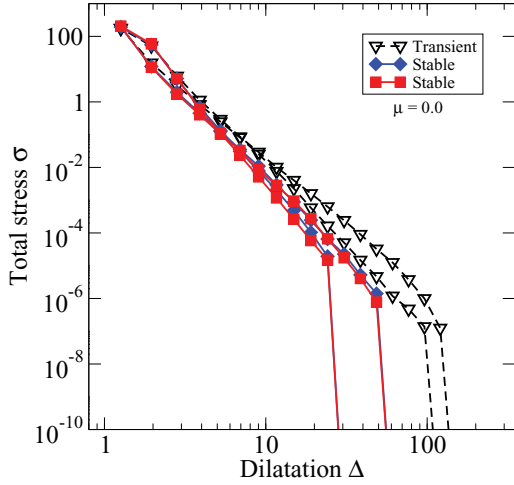


FIG. 4. (Color online) Total stress produced during compaction and expansion of a random fiber network without friction ($\mu = 0$) during the transient and stable cycles.

by the bending mode at large Δ (low densities). As the network is compacted, the axial mode contribution increases faster than the bending mode contribution, and eventually takes over ($\sigma_{bending} \sim \Delta^{-5.09}$; $\sigma_{axial} \sim \Delta^{-7.35}$). The crossover happens at $\Delta = 2.44$. This transition is shown in the inset, where the ratios of the strain energy density associated with fiber bending, to the total strain ($\dot{U}_{bending} : \dot{U}_{total}$), and the corresponding ratio for the axial mode are shown as a function of the dilatation strain. This observation of a larger scaling exponent of σ_{axial} with Δ suggests an explanation for the larger exponents observed in experiments. If the system behavior is dominated by the axial deformation mode, the total stress should follow the trend set by σ_{axial} . This issue is discussed in more detail later in this section.

The contribution of $\sigma_{contact}$ is at least an order of magnitude lower than the contribution of the other two components at all dilatations, and its scaling exponent is similar to the scaling exponent of $\sigma_{bending}$. This is because the contact forces,

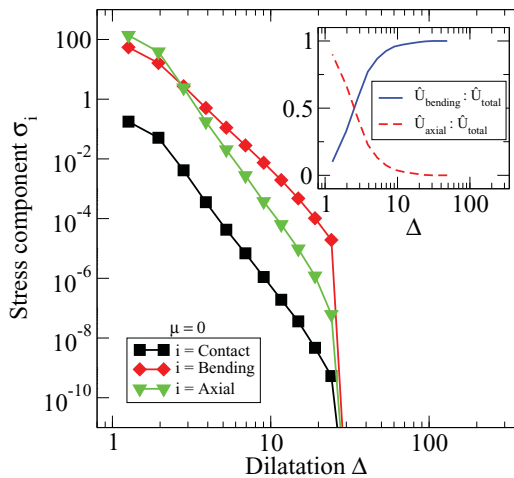


FIG. 5. (Color online) Partition of total stress into contact, axial, and bending components during the loading portion of a stable cycle for a system with $\mu = 0$. (Inset) Ratios of energy density associated with bending and axial modes to the total energy density.

perpendicular to the fiber axis, are responsible for bending. The dominance of the bending mode at low densities, and the transition from bending-dominated to axial-dominated deformation as the network density increases has been observed in two-dimensional (2D) bonded networks of phantom fibers (fibers that can cross each other) [39,40]. In 2D systems, the transition is controlled by both the density, and the ratio of the bending to axial stiffness of fibers, $l_b^2 = EI/EA$. The bending mode dominates at small densities and for small l_b (long, slender fiber segments). Our data show that nonbonded networks behave qualitatively in a similar manner.

We also compute the bulk modulus, $K = \partial\sigma/\partial\Delta$, obtained from the total stress of the loading branch of the stable cycle, in Fig. 4(a). The fits obtained by computing the appropriate derivatives are $K \sim \Delta^{-6.25}$, which is equivalent to $K \sim \rho^{4.75}$. Experimentally, the Young's modulus, as measured from the slope of the unloading branch of the stress-strain curve, varies with the density as $E \sim \rho^m$, where, for experiments reported by Masse *et al.* [21], m increases from 3 to approximately 4.5 as the sample mass increases. Cross-linked networks subjected to smaller deformations exhibit more complex behavior, where if the density and/or l_b is large, the network shear modulus scales linearly with density. This is also the prediction of the affine or effective medium theories of network mechanics, as well as the behavior of open cell networks and of rubber [41]. This type of response is denoted as ‘‘affine.’’ When the density and/or l_b is small, the shear modulus scales as $G \sim \rho^m$, with m being quite large ($m = 6.67$ in [39]). This regime is denoted as ‘‘nonaffine’’ and, as the name suggests, theories based on the affine motion of network segments do not apply.

To further investigate the effect of $l_b = \sqrt{k_b/k_a}$ on the stress-strain curve, k_b is varied while keeping k_a constant. The stiffness k_a is not modified in order to keep the effective fiber surface roughness unchanged. Also, the diameter of the fiber, d , is kept constant, so that the excluded volume contribution remains the same in all these systems. For isotropic cylindrical fibers, with $l_b = d/4$, this modification is artificial but allows us to decouple the effect of fiber bending stiffness and fiber aspect ratio on the stress-strain behavior of the network. The issue is relevant for fibers made from anisotropic materials. Figure 6(a) shows the loading branch of the stable cycle of systems with k_b one order of magnitude larger, and two orders of magnitude smaller than the value used in all other simulations, where $k_b = 29.31\hat{e}$. The energy partition in bending and axial modes for these systems is shown in Fig. 6(b). Reducing k_b by two orders of magnitude enables more energy to be stored in the bending mode, and the stress-dilatation curve follows a scaling of $\sigma \sim \Delta^5$, which corresponds to $\sigma \sim \rho^3$, thereby recovering the prediction from van Wyk's theory [23], which takes into account only the bending stiffness of the fibers.

Increasing the bending stiffness by an order of magnitude, on the other hand, cripples the bending mode and stores more energy in the axial mode. This corresponds to a much higher slope of the σ - Δ curve, which is comparable to the slope of the axial component in Fig. 5. This result can be related to a number of experimental observations. Poquillon *et al.* [19] performed compression on two types of steel wool with l_b^2 differing by an order of magnitude. The system with small l_b follows the relationship $\sigma \sim \rho^{2.5}$, while the one with larger l_b follows

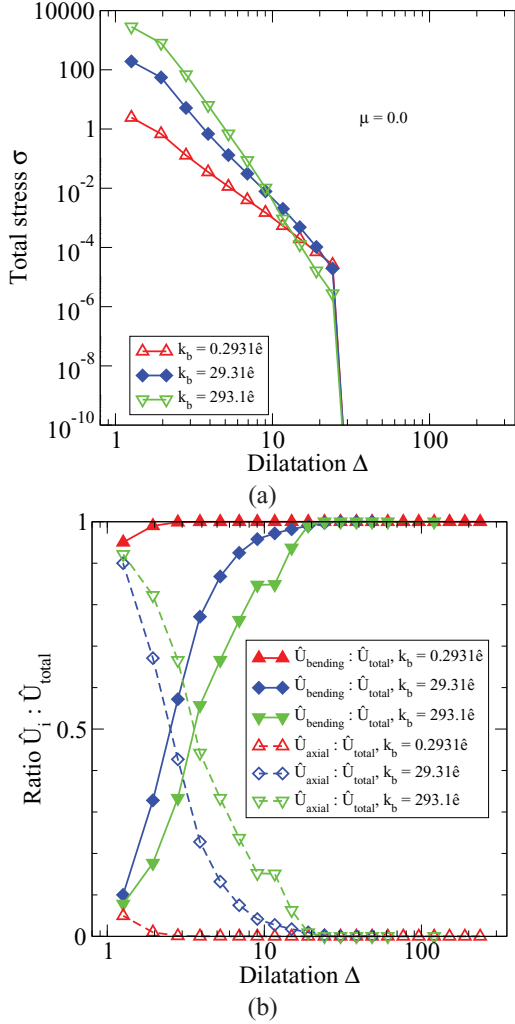


FIG. 6. (Color online) (a) Total stress and (b) partition of energies, during loading in networks with the original, and artificially modified bending stiffness. Reduction in bending stiffness by two orders of magnitude produces a σ - Δ scaling that matches earlier theories [23,26].

$\sigma \sim \rho^{3.93}$. Data are also reported for wads of vegetable horse-hair composed of mixed fibers, with diameters ranging from 20 to 2000 μm , which lead to a much higher exponent, $\sigma \sim \rho^{5.48}$.

Looking at the effect of fiber-fiber friction, Fig. 7 shows the total stress as a function of dilatation strain for the reference system with $\mu = 0$ and for systems with $\mu = 0.1$ and $\mu = 1$. Friction does not modify the functional form of the stress-strain relationship, but increases the value of stress. The increase is rather small, and for a more realistic friction coefficient, $\mu = 0.1$, the curve is essentially indistinguishable from that for $\mu = 0$ in this log-log plot.

B. Sliding at contact points

The foregoing discussion suggests that the mechanical behavior of a system of nonbonded fibers in the network regime is determined by a number of factors such as (a) fiber bending, which dominates at low densities; (b) axial deformation of fibers, which dominates at higher densities;

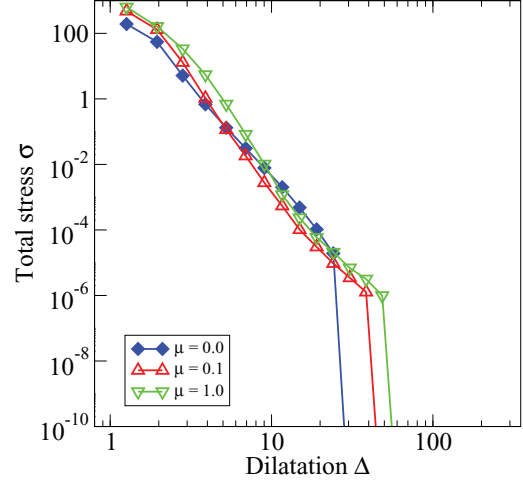


FIG. 7. (Color online) Stress-strain curves for networks with $\mu \in [0.0, 0.1, 1.0]$. Introduction of friction slightly modifies the magnitude of stress.

(c) formation of new contacts during compaction; (d) relative fiber sliding at contacts and subsequent fiber rearrangement; (e) friction at contacts. The theories of van Wyk [23] and Toll [26] account for fiber bending and for the increase of the number of contacts as the wad is compressed. We have seen that the axial contribution may increase the absolute value of the σ - Δ power law exponent, relative to the exponent predicted by considering only the bending deformation of the fibers (Fig. 5). Friction has negligible effect on these exponents (Fig. 7). In this section we investigate the importance of relative fiber sliding in defining the constitutive response of the ensemble of fibers.

To identify the magnitude of sliding events, the following procedure is employed. A configuration in the network regime from the stable loading branch of the system is selected and taken as the reference ($\Delta = 5.21$). All contacts in this configuration are identified and then the system is subjected to compression in small increments (each step corresponds to a change of the simulation box size by 0.16 δ , i.e., approximately $d/7$). The relative motion of fibers is monitored at all contacts. Figure 8 shows a schematic of a contact between two fibers and the quantities of interest. The rectangle denotes a fiber viewed

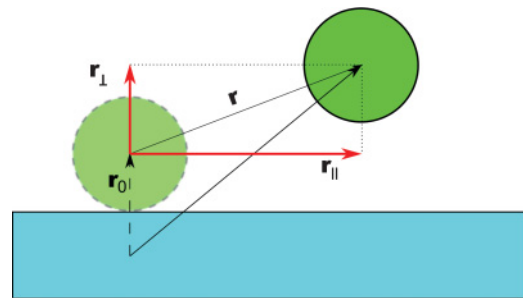


FIG. 8. (Color online) Schematic illustrating the relative motion of two fibers and the definition of separation and sliding vectors. The axes of the two fibers in contact are assumed to be perpendicular to each other, but this is not a requirement. The rectangle is a fiber viewed sideways, while the circles indicate a second fiber viewed along its axis.

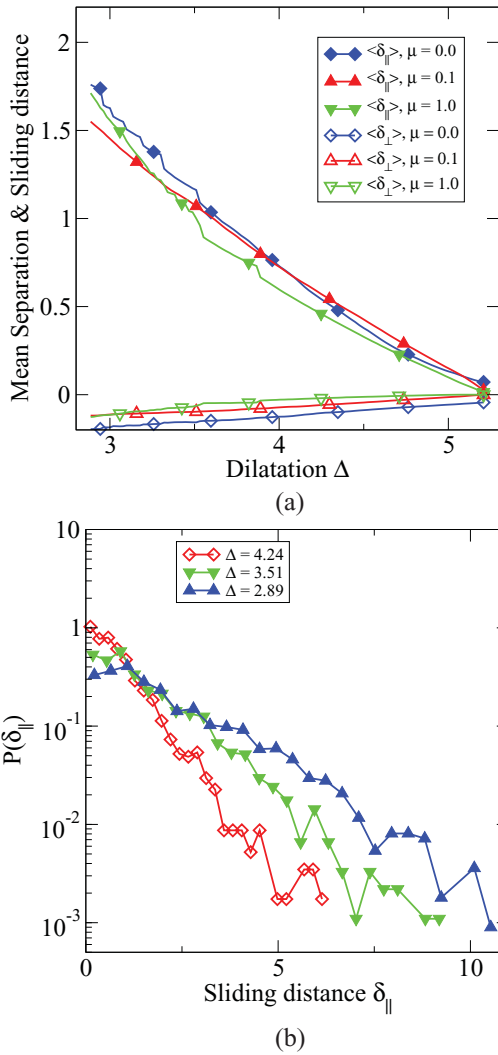


FIG. 9. (Color online) Contacts formed at an arbitrarily selected configuration with $\Delta = 5.21$ are tracked. (a) Mean separation $\langle \delta_{\perp} \rangle$ and mean sliding $\langle \delta_{\parallel} \rangle$ distance at contacts. (b) For the system with $\mu = 0$, PDF of sliding distances, $P(\delta_{\parallel})$, between the reference configuration with $\Delta = 5.21$ and configurations at various values of Δ . These PDFs are exponential, consistent with a Poisson process.

sideways, while the circles indicate a second fiber viewed along its axis. While the two fibers shown in the schematic are perpendicular to each other, this is not a requirement for the computations. The broken and solid circles indicate the second fiber in the reference and deformed configurations, respectively. The relative motion is defined by the vector \mathbf{r} . This vector is decomposed in two orthogonal components: \mathbf{r}_{\perp} , which is perpendicular to, and \mathbf{r}_{\parallel} , which is parallel to, the tangent at the point of contact between the two fibers. The magnitudes of these orthogonal vectors are denoted as δ_{\parallel} , which represents the relative sliding, and δ_{\perp} , which represents the separation. A negative value for δ_{\perp} indicates that fibers press against each other at the contact point.

Figure 9(a) shows the variation of the mean sliding and separation during loading from the reference configuration. The separation δ_{\perp} is negative, indicating that, on average, fibers in contact in the reference configuration remain in

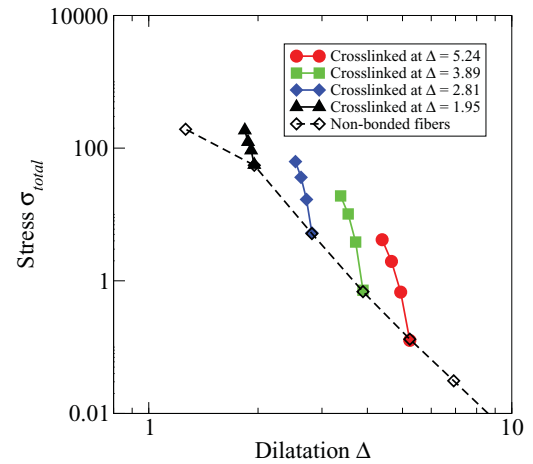


FIG. 10. (Color online) Total stress obtained when compressing a cross-linked network, shown as solid symbols with solid lines. Open symbols joined by a broken line show part of the loading branch of the stable cycle, from Fig. 4(a). Cross links are introduced at fiber contacts at various stages of compaction (Δ) in separate simulations.

contact. However, the amount of sliding, δ_{\parallel} , is significant, and increases almost linearly with Δ . These conclusions remain valid in systems with friction. The relative sliding decreases to some extent as the friction coefficient increases. We also see that sliding occurs in bursts which involve multiple neighboring contacts, a behavior similar to that leading to intermittent dynamics and avalanches in other discrete systems such as granular media and large populations of interacting dislocations. The analysis of the statistics of these bursts and associated phenomenology is deferred to a subsequent publication. The variation of δ_{\parallel} with Δ in Fig. 9 exhibits only traces of these events due to the smoothing induced by averaging over all contacts and over neighboring snapshots of the simulation. Figure 9(b) shows the PDF of δ_{\parallel} obtained at a few Δ values indicated in the legend. The distribution is exponential, which indicates that the sliding magnitudes are random.

In order to determine the importance of such relative fiber rearrangements on the overall behavior of the network, fibers that were in contact in the reference configuration were cross linked at their contact points by introducing harmonic bonds with the stiff potential given in Eq. (4). This synthetic cross-linking process effectively prevents sliding and opening of contacts, but allows the formation of new contacts. The cross-linked network was then subjected to triaxial compression. The stress was evaluated without taking the contribution of the new cross links into account. Figure 10 shows the stress-strain response of the nonbonded network (open symbols), and of four different networks, in which cross links were introduced at $\Delta \in \{4.94, 3.71, 2.72, 1.91\}$. The cross-linked networks are all significantly stiffer than the original nonbonded network. This observation shows that sliding is an important component of the physics in these systems and constitutive models aimed at predicting the average global response of the network must take it into account. This observation has also been made by Carnaby and Pan [25], who compare their model, which takes sliding into account, with experimental data and a model by Lee and Lee [18].

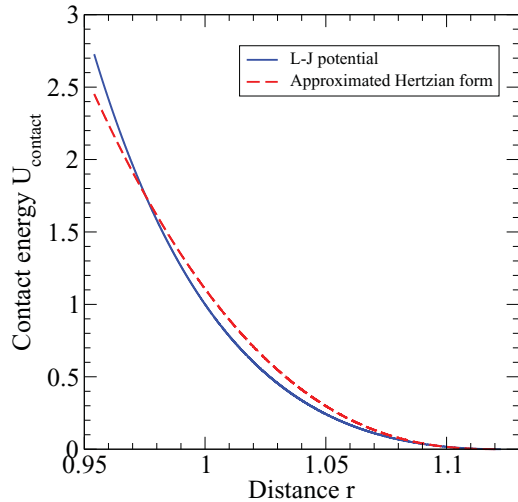


FIG. 11. (Color online) Least-squares fit of the approximated Hertzian form of the Lennard-Jones potential with $C_1 = 210.86$.

IV. CONCLUSIONS

The macroscopic behavior of an ensemble of random, nonbonded fiber networks was examined using a coarse-grained bead-spring model that was calibrated to replicate continuous cylindrical fibers. The ensemble was subjected to triaxial compression and expansion. We observed hysteretic behavior associated with fiber rearrangements. We see that the dependence of the Cauchy stress on density is a power law. The exponent of this power law is controlled by *both* bending and axial deformation modes. At low densities, the response of the network is bending dominated, while at higher densities, it is axial dominated. Friction does not appreciably change the exponent of the stress-strain function. Relative sliding of fibers is an important component of the physics associated with the macroscopic response of the network. We have demonstrated that constitutive models for the response of an ensemble of fibers that consider bending and formation of new contacts should also incorporate the effect of contributions from relative fiber sliding and that of the axial deformation modes.

ACKNOWLEDGMENTS

Part of the simulations were executed on the SUR BlueGene/L at Rensselaer Polytechnic Institute, which is supported

by Grant No. 0420703 and a gift by the IBM Corporation of a BlueGene/L computer. Thanks to Tim Wickberg for his expert maintenance of the SCOREC computing clusters.

APPENDIX: CHOICE OF INTERACTION POTENTIAL COEFFICIENTS

The discrete bead-spring model is calibrated to represent cylindrical fibers described by the Euler-Bernoulli beam theory. The calibration is based on requiring that the energies computed using Eqs. (2), (3), and (4) for the discrete model are equivalent to the strain energy stored in the bending and axial modes, and to the strain energy stored due to the deformation of the material at contact points in the continuum model of the fiber. Requiring that Eq. (3) provides a value equal to the energy stored in a cylinder of length d subjected to axial loading leads to an expression for the axial stiffness, and similarly requiring that Eq. (4) provides a value equivalent to the energy stored in a fiber subjected to bending leads to an expression for the bending stiffness. These expressions are

$$k_a = \frac{\pi}{4} E d, \tag{A1}$$

$$k_b = \frac{\pi}{64} E d^3, \tag{A2}$$

where E is Young’s modulus of the fiber material.

Equation (2) describing the contact between beads should provide values equivalent to those computed using Hertz theory [42] for the contact of two cylinders of equal diameter d . In this theory, the energy stored at a contact for which the distance between centers of the two fibers involved is r is given by

$$U_{contact} = \frac{2E}{3(1-\nu^2)} \sqrt{\frac{d}{2}} (d-r)^{5/2}. \tag{A3}$$

We fit the Lennard-Jones potential of Eq. (2) close to the cutoff $r = r_c$ with the function $C_1(d-r)^{5/2}\hat{\epsilon}$. A least squares fit in the range $r \in [0.85d : d]$ yields $C_1 = 210.86$. The fit obtained is shown in Fig. 11. We can further take $1 - \nu^2 \approx 1$ for realistic values of ν and obtain the value for the Young’s modulus as $E = 420.4\hat{\epsilon}\delta^{-3}$, which yields the coefficients entering the axial and bending potentials in Eqs. (3) and (4) as $k_a = 372.2\hat{\epsilon}/\delta^2$ and $k_b = 29.31\hat{\epsilon}$.

[1] H. M. James and E. Guth, *J. Chem. Phys.* **11**, 455 (1943).
 [2] L. R. G. Treloar, *The Physics of Rubber Elasticity* (Clarendon Press, Oxford, 1975).
 [3] P. J. Flory, *Principles of Polymer Chemistry* (Cornell University Press, Ithaca, NY, 1953).
 [4] I. Qashou, H. V. Tafreshi, and B. Pourdeyhimi, *J. Eng. Fibers Fabr.* **4**, 9 (2009).
 [5] P. Gibson, H. Schreuder Gibson, and D. Rivin, *Colloids Surf. A* **187-188**, 469 (2001).
 [6] Y. Shoshani and Y. Yakubov, *Text. Res. J.* **69**, 519 (1999).
 [7] L. Huang, R. A. McMillan, R. P. Apkarian, B. Pourdeyhimi, V. P. Conticello, and E. L. Chaikof, *Macromolecules* **33**, 2989 (2000).
 [8] C. A. Pezowicz, P. A. Robertson, and N. D. Broom, *J. Anat.* **208**, 317 (2006).
 [9] M. L. Schollum, P. A. Robertson, and N. D. Broom, *J. Anat.* **214**, 805 (2009).
 [10] K. Kroy, *Curr. Opin. Colloid Interface Sci.* **11**, 56 (2006).

- [11] T. D. Pollard and G. G. Borisy, *Cell* **112**, 453 (2003).
- [12] E. M. Reichl, J. C. Effler, and D. N. Robinson, *Trends Cell Biol.* **15**, 200 (2005).
- [13] Y. Takano and A. Sakanishi, *Biorheology* **25**, 123 (1988).
- [14] E. K. F. Yim, E. M. Darling, K. Kulangara, F. Guilak, and K. W. Leong, *Biomaterials* **31**, 1299 (2010).
- [15] M. Rigdahl and H. Hollmark, in *Paper Structure and Properties*, edited by J. A. Bristow and P. Koeth (Dekker, New York, 1986), p. 241.
- [16] C. T. J. Dodson and P. Herdman, in *Handbook of Paper Science*, edited by H. F. Rance (Elsevier, Amsterdam, 1980), Vol. 2, p. 71.
- [17] R. C. Picu, *Soft Matter* (2007), doi: 10.1039/clsm05022b.
- [18] D. H. Lee and J. K. Lee, in *Objective Measurement: Applications to Product Design and Process Control*, edited by A. Kawabata, R. Postle, and M. Niwa (Textile Manufacturing Society of Japan, Osaka, 1985), pp. 613–622.
- [19] D. Poquillon, B. Viguier, and E. Andrieu, *J. Mater. Sci.* **40**, 5963 (2005).
- [20] S. Bergonnier, F. Hild, J. B. Rieunier, and S. Roux, *J. Mater. Sci.* **40**, 5949 (2005).
- [21] J. Masse, L. Salvo, D. Rodney, Y. Brechet, and O. Bouaziz, *Scr. Mater.* **54**, 1383 (2006).
- [22] D. Poquillon, B. Viguier, and E. Andrieu, *18 Congres Francais de Mecanique* (Association Francaise de Mecanique, 2007).
- [23] C. M. van Wyk, *J. Text. Inst.* **37**, T285 (1946).
- [24] O. Kallmes and H. Corte, *TAPPI J.* **43**, 737 (1960).
- [25] G. A. Carnaby and N. Pan, *Text. Res. J.* **59**, 275 (1989).
- [26] S. Toll, *Polym. Eng. Sci.* **38**, 1337 (1998).
- [27] M. Baudequin, G. Ryschenkow, and S. Roux, *Eur. Phys. J. B* **12**, 157 (1999).
- [28] D. Rodney, M. Fivel, and R. Dendievel, *Phys. Rev. Lett.* **95**, 108004 (2005).
- [29] D. Durville, *J. Mater. Sci.* **40**, 5941 (2005).
- [30] B. Pourdeyhimi, B. Maze, and H. V. Tafreshi, *J. Eng. Fibers Fabr.* **1**, 47 (2006).
- [31] R. C. Picu and M. C. Pavel, *Macromolecules* **36**, 9205 (2003).
- [32] A. Rakshit and R. C. Picu, *J. Chem. Phys.* **125**, 164907 (2006).
- [33] R. C. Picu and A. Rakshit, *J. Chem. Phys.* **127**, 144909 (2007).
- [34] S. Plimpton, *J. Comput. Phys.* **117**, 1 (1995).
- [35] S. Feng and P. N. Sen, *Phys. Rev. Lett.* **52**, 216 (1984).
- [36] A. L. R. Bug, S. A. Safran, and I. Webman, *Phys. Rev. Lett.* **54**, 1412 (1985).
- [37] I. Balberg, N. Binenbaum, and N. Wagner, *Phys. Rev. Lett.* **52**, 1465 (1984).
- [38] S. R. Williams and A. P. Philipse, *Phys. Rev. E* **67**, 051301 (2003).
- [39] J. Wilhelm and E. Frey, *Phys. Rev. Lett.* **91**, 108103 (2003).
- [40] G. E. Pike and C. H. Seager, *Phys. Rev. B* **10**, 1421 (1974).
- [41] L. J. Gibson and M. F. Ashby, *Cellular Solids: Structure and Properties* (Pergamon, Oxford, 1988).
- [42] H. Hertz, *J. Reine Angew. Math.* **92**, 156 (1881).